Image-Based Visual-Impedance Control of a Dual-Arm Aerial Manipulator

Vincenzo Lippiello, Giuseppe Andrea Fontanelli, and Fabio Ruggiero

***Abstract*—Three new image-based visual-impedance control laws are proposed in this paper allowing physical interaction of a dual-arm unmanned aerial manipulator equipped with a camera and a force/torque sensor. Namely, two first-order impedance behaviours are designed based on the transpose and the inverse of the system Jacobian matrix, respectively, while a second-order impedance behaviour is carried out as well. Visual information is employed both to coordinate the camera motion in an eye-in-hand configuration with the assigned task executed by the other robot arm, and to define the elastic wrench component of the proposed hybrid impedance equations directly in the image plane.**

***Index Terms*—Aerial Systems: Perception and Autonom, force control, Visual Servoing.**

I. Introduction

UNMANNED aerial vehicles (UAVs) are employed in several "passive" tasks such as surveillance, inspection, remote sensing, and so on. Recently, these vehicles have also been tested in "active" tasks like grasping, transporting and, lately, manipulation. Grasping objects during the flight requires to cope with several issues mainly related to the unstable dynamics of the vehicle and the coupling effects due to the carried object [1]. UAVs equipped with robot arms are a promising solution providing the capability of executing dexterous manipulation tasks.

The mechatronic design of a robotic manipulator that is meant mounted on a UAV and to be used in industrial applications, for both aerial inspection by contact and aerial manipulation, is proposed in [2]. Similarly, the design, modeling and control of a 5 degrees of freedom (DoFs) light-weight robot manipulator for small-scale UAV has been proposed in [3]. Recently, the design of a dual-arm aerial manipulator consisting of a multi-rotor platform with an ultra-lightweight human-size dual arm prototype and its control system have been described in [4]. Such a solution is referred to as Unmanned Aerial Manipulator (UAM) and is considered in this paper. Sophisticated controllers are needed for UAMs to stabilize physical interaction with the environment. In [5], an interaction control has been proposed allowing a UAM to track a desired normal force while moving on a wall. An impedance control law able to govern the DoFs of a UAM is proposed in [6], while a Cartesian impedance control law has been presented in [7] and [8], where a dynamic relationship between external forces, specified in terms of Cartesian space coordinates, has been provided. A nonlinear adaptive impedance controller is proposed in [9] allowing the control of the manipulator's end-effector Cartesian impedance to have a stable interaction. In [10], a multi-level impedance control scheme is composed of a trajectory generator and an impedance filter that modifies the trajectory to achieve a complaint behaviour in the task space.

The interaction of a robot arm with a rigid object of known geometry and unknown (time-varying) pose is considered in [11]. An algorithm for the pose estimation of the object has been proposed, based on visual data provided by a camera as well as on forces and moments measured during the interaction with the environment. Differently from what is proposed in this paper, visual and force control are not simultaneously employed in a unique control law to achieve an impedance behaviour.

In this paper, a UAM equipped with a dual-arm robot system is considered. A camera is mounted in one hand, while the other hand is endowed with a wrist force/torque sensor and holds an object (peg) to be mounted in a structure (hole) fixed on the ground. The peg-in-hole is just an explanatory case study: the approach can be in principle extended to other tasks. Novel visual-impedance control laws have been designed in a common control framework: two first-order impedance control laws based on the transpose and the inverse of the system Jacobian matrix are proposed together with a complete second-order visual-impedance control law. Visual information is employed to coordinate the camera motion, fixed in one hand of the robot, with the assigned task executed with the second arm carrying an object. In an innovative way, for each control law a suitable visual error is defined directly in the image plane generating an elastic wrench component to nullify the pose error with a compliant interaction behaviour. Simulations bolster the effectiveness of the proposed techniques.

II. Modeling

Figure 1 shows an example of the addressed system. This section describes the (differential) kinematics and the dynamic model of a dual-arm UAM. Finally, the camera model and its differential kinematics are presented.

Manuscript received: 9, 7, 2017; Revised 11, 22, 2017; Accepted 2, 8, 2018.

This paper was recommended for publication by Editor Jonathan Roberts upon evaluation of the Associate Editor and Reviewers' comments.

This work was supported by the AEROARMS project, funded by the European Community's H2020 Framework Programme under Grant ICT-644271. The authors are solely responsible for its content. It does not represent the opinion of the European Community, which is not responsible for any use that might be made of the information contained therein.

Authors are with the CREATE Consortium and with the PRISMA Laboratory, Department of Electrical Engineering and Information Technology, University of Naples Federico II, 80125, Naples, Italy.

Corresponding author: V. Lippiello, email: lippiello@unina.it.

Digital Object Identifier (DOI): see top of this page.

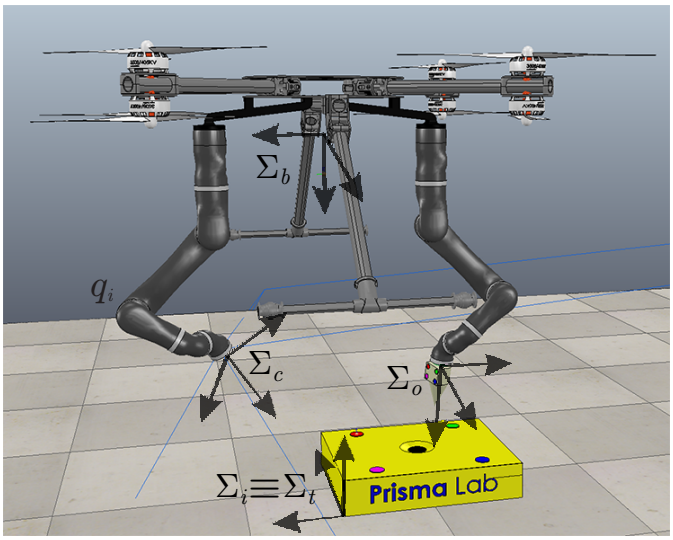

Fig. 1. Dual-arm UAM and corresponding reference frames.

A. Kinematic model

The reference frames adopted to model the proposed system are shown in Figure 1. The inertial reference frame has the z-axis upward and is labeled with Σ_i and, without loss of generality, is coincident with the reference frame Σ_t attached to the target fixed at the ground.

The reference frame Σ_b is fixed at the center of mass of the vehicle base and has the z-axis downward. The position and orientation of Σ_b with respect to Σ_i are denoted by $\boldsymbol{o}_b \in \mathbb{R}^3$ and $\boldsymbol{R}_b(\boldsymbol{\phi}_b) \in \mathrm{SO}(3)$, respectively, where $\boldsymbol{\phi}_b$ contains the ZYX Euler angles corresponding to the rotation matrix $\boldsymbol{R}_b$.

The two attached robotic manipulators are made of a succession of links and actuated joints, whose positions are described through the joint vectors $\boldsymbol{\varrho}_c \in \mathbb{R}^{n_c}$ and $\boldsymbol{\varrho}_o \in \mathbb{R}^{n_o}$, respectively. A camera is mounted on one arm of the UAM, and its reference frame Σ_c is coincident with the corresponding end-effector reference frame, with the z-axis (i.e., the *optical axis*) coincident with the outgoing approaching axis. The pose (position and orientation) of Σ_c with respect to Σ_b is $\boldsymbol{o}_c^b(\boldsymbol{\varrho}_c) \in \mathbb{R}^3$ and $\boldsymbol{R}_c^b(\boldsymbol{\varrho}_c) \in \mathrm{SO}(3)$, respectively. The second arm carries an object with a reference frame Σ_o supposed to be coincident with its end-effector reference frame. Similarly, the corresponding position and orientation of Σ_o with respect to Σ_b are $\boldsymbol{o}_o^b(\boldsymbol{\varrho}_o) \in \mathbb{R}^3$ and $\boldsymbol{R}_o^b(\boldsymbol{\varrho}_o) \in \mathrm{SO}(3)$, respectively.

Let $\boldsymbol{\xi} = \begin{bmatrix} \boldsymbol{o}_b^\top & \boldsymbol{\phi}_b^\top & \boldsymbol{\varrho}_c^\top & \boldsymbol{\varrho}_o^\top \end{bmatrix}^\top \in \mathbb{R}^n$ be the generalized vector of joint positions of the whole system, with $n = 6 + n_c + n_o$. If the orientation of the end-effectors of the robot arms are expressed in terms of a nonsingular representation employing quaternions $\boldsymbol{q}_c \in \mathbb{R}^4$ and $\boldsymbol{q}_o \in \mathbb{R}^4$, the Cartesian pose of the camera and of the transported object can be represented through the pose vector $\boldsymbol{x} = \begin{bmatrix} \boldsymbol{o}_c^\top & \boldsymbol{q}_c^\top & \boldsymbol{o}_o^\top & \boldsymbol{q}_o^\top \end{bmatrix}^\top = \boldsymbol{k}(\boldsymbol{\xi}) \in \mathbb{R}^{14}$, where $\boldsymbol{k}(\cdot)$ is a nonlinear vectorial function.

B. Differential kinematic model

Let $\boldsymbol{v}_b = \begin{bmatrix} \dot{\boldsymbol{o}}_b^\top & \boldsymbol{\omega}_b^\top \end{bmatrix}^\top \in \mathbb{R}^6$ be the twist collecting the absolute linear $\dot{\boldsymbol{o}}_b$ and angular $\boldsymbol{\omega}_b$ velocities of Σ_b with respect to Σ_i. By denoting with $\dot{\boldsymbol{\phi}}_b$ the time derivative of $\boldsymbol{\phi}_b$, the corresponding relation with $\boldsymbol{\omega}_b$ is

$$\boldsymbol{\omega}_b = \boldsymbol{T}_b(\boldsymbol{\phi}_b)\dot{\boldsymbol{\phi}}_b, \tag{1}$$

where $\boldsymbol{T}_b \in \mathbb{R}^{3\times3}$ is a transformation matrix depending on the chosen family of Euler angles [12]. This matrix suffers of the so called *representation singularities*, i.e., it becomes singular for some isolated values of $\boldsymbol{\phi}_b$. For the ZYX Euler angles, representation singularities appear if the z-axes of Σ_b and Σ_i becomes orthogonal, which is never an useful configuration for a UAM, which typically is in a quasi-stationary flight.

Let $\boldsymbol{v}_c^b = \begin{bmatrix} \dot{\boldsymbol{o}}_c^{b\top} & \boldsymbol{\omega}_c^{b\top} \end{bmatrix}^\top$ be the twist of Σ_c with respect to Σ_b, where $\dot{\boldsymbol{o}}_c^b \in \mathbb{R}^3$ and $\boldsymbol{\omega}_c^b \in \mathbb{R}^3$ are its linear and angular velocity components, respectively. The mapping between $\boldsymbol{v}_c^b$ and the time derivative $\dot{\boldsymbol{\varrho}}_c$ of the joint positions of the corresponding arm is given by

$$\boldsymbol{v}_c^b = \boldsymbol{J}_c^b(\boldsymbol{\varrho}_c)\dot{\boldsymbol{\varrho}}_c, \tag{2}$$

where $\boldsymbol{J}_c^b \in \mathbb{R}^{6\times n_c}$ is the so-called *geometric Jacobian* of the robot arm fitted with the camera. In a similar way, the twist of Σ_o with respect to Σ_b is

$$\boldsymbol{v}_o^b = \begin{bmatrix} \dot{\boldsymbol{o}}_o^{b\top} & \boldsymbol{\omega}_o^{b\top} \end{bmatrix}^\top = \boldsymbol{J}_o^b(\boldsymbol{\varrho}_o)\dot{\boldsymbol{\varrho}}_o, \tag{3}$$

where $\boldsymbol{J}_o^b \in \mathbb{R}^{6\times n_o}$ is the geometric Jacobian of the robot arm carrying the object.

The vector $\boldsymbol{v} = \begin{bmatrix} \boldsymbol{v}_c^\top & \boldsymbol{v}_o^\top \end{bmatrix}^\top$ can be considered if one is interested to control only the arms's end-effectors. The corresponding differential kinematic equation is

$$\boldsymbol{v} = \boldsymbol{J}(\boldsymbol{\xi})\dot{\boldsymbol{\xi}}, \tag{4}$$

where $\boldsymbol{J} = \mathrm{diag}(\bar{\boldsymbol{R}}_b\boldsymbol{J}_c^b, \bar{\boldsymbol{R}}_b\boldsymbol{J}_o^b)$, with $\bar{\boldsymbol{R}}_b = \mathrm{diag}(\boldsymbol{R}_b, \boldsymbol{R}_b)$, is the new geometric Jacobian. In such a case, the intrinsic redundancy of the system can be exploited to control the behaviour of the vehicle base.

C. Dynamic model

The dynamic model of the UAM can be computed by considering the *Euler-Lagrange* formulation [12]. The system dynamics can be expressed as follows

$$\boldsymbol{B}(\boldsymbol{\xi})\ddot{\boldsymbol{\xi}} + \boldsymbol{C}(\boldsymbol{\xi}, \dot{\boldsymbol{\xi}})\dot{\boldsymbol{\xi}} + \boldsymbol{g}(\boldsymbol{\xi}) = \boldsymbol{u} - \boldsymbol{u}_e, \tag{5}$$

where $\boldsymbol{B} \in \mathbb{R}^{n\times n}$ is the symmetric and positive definite inertia matrix, $\boldsymbol{C} \in \mathbb{R}^{n\times n}$ represents centrifugal and Coriolis effects, $\boldsymbol{g} \in \mathbb{R}^n$ is the vector of gravitational terms, $\boldsymbol{u} \in \mathbb{R}^n$ is the input vector, and $\boldsymbol{u}_e = \boldsymbol{J}^\top(\boldsymbol{\xi})\boldsymbol{h}_e \in \mathbb{R}^n$ shapes the effects of generalized external wrench $\boldsymbol{h}_e = \begin{bmatrix} \boldsymbol{0}_6^\top & \boldsymbol{h}_o^\top \end{bmatrix}^\top$ at joint level, with $\boldsymbol{h}_o \in \mathbb{R}^6$ the external wrench acting on the arm carrying the object, and $\boldsymbol{0}_\times$ a null vector of $\times$ elements. See [7], [8] for more details in case of a single-arm UAM.

By initially neglecting aerodynamic effects, which are very complex to be explicitly modeled [13], the vector $\boldsymbol{u}$ can be rewritten as follows

$$\boldsymbol{u} = \boldsymbol{M}\boldsymbol{N}\boldsymbol{f} = \boldsymbol{G}\boldsymbol{f}, \tag{6}$$

where $\boldsymbol{G} = \boldsymbol{M}\boldsymbol{N}$, $\boldsymbol{f} = \begin{bmatrix} \boldsymbol{f}_b^\top & \boldsymbol{\tau}_c^\top & \boldsymbol{\tau}_o^\top \end{bmatrix}^\top$, with $\boldsymbol{f}_b \in \mathbb{R}^4$ the vector of the input forces provided by the quadrotor propellers,

and $\boldsymbol{\tau}_c \in \mathbb{R}^{n_c}$ and $\boldsymbol{\tau}_o \in \mathbb{R}^{n_o}$ the robot manipulators joint torques, $\boldsymbol{M} = \mathrm{diag}(\boldsymbol{R}_b, \boldsymbol{T}_b^\top \boldsymbol{R}_b, \boldsymbol{I}_{n_c+n_o}) \in \mathbb{R}^{n\times n}$, $\boldsymbol{N} = \mathrm{diag}(\boldsymbol{\Omega}, \boldsymbol{I}_{n_c+n_o}) \in \mathbb{R}^{n\times 4+n_c+n_o}$, with the constant matrix $\boldsymbol{\Omega} \in \mathbb{R}^{6\times 4}$ described in [7] and $\boldsymbol{I}_\alpha \in \mathbb{R}^{\alpha\times\alpha}$ the identity matrix. Since $\boldsymbol{G}^\top\boldsymbol{G}$ is invertible except for the representation singularities, equation (6) can be inverted yielding $\boldsymbol{f} = \boldsymbol{G}^\dagger \boldsymbol{u}$, where the symbol † denotes the pseudo-inverse of a matrix.

D. Camera model

The *pin-hole* camera model is considered. Let $\boldsymbol{p}^c = \begin{bmatrix} x^c & y^c & z^c \end{bmatrix}^\top \in \mathbb{R}^3$ be the position of an observed point in Σ_c. The corresponding projection onto the *normalized image plane* —the plane at a distance of 1m from Σ_c along the optical axis— is called *point image feature* and can be computed as follows

$$\boldsymbol{s} = \begin{bmatrix} X \\ Y \end{bmatrix} = \frac{1}{z^c} \begin{bmatrix} x^c \\ y^c \end{bmatrix}, \tag{7}$$

where X and Y are the coordinates of $\boldsymbol{s}$.

E. Differential kinematics of the target's image features

Let the fixed target be endowed with a set of m_t visible feature points whose position in Σ_t are $\boldsymbol{p}_{t,i}^t$, with $i = 1, \ldots, m_t$. Let $\boldsymbol{s}_{t,i} = \begin{bmatrix} X_{t,i} & Y_{t,i} \end{bmatrix}^\mathrm{T} \in \mathbb{R}^2$ be the image feature vector corresponding to the i-th target point. The time variation of $\boldsymbol{s}_{t,i}$ is only affected by the camera motion [14]:

$$\dot{\boldsymbol{s}}_{t,i} = \begin{bmatrix} \dot{X}_{t,i} \\ \dot{Y}_{t,i} \end{bmatrix} = \boldsymbol{L}_{t,i} \bar{\boldsymbol{R}}_c^\top \boldsymbol{v}_c = \boldsymbol{J}_{t,i} \boldsymbol{v}_c, \tag{8}$$

where

$$\boldsymbol{L}_{t,i} = \begin{bmatrix} -\frac{1}{z_{t,i}^c} & 0 & \frac{X_{t,i}}{z_{t,i}^c} & X_{t,i}Y_{t,i} & -1-X_{t,i}^2 & Y_{t,i} \\ 0 & -\frac{1}{z_{t,i}^c} & \frac{Y_{t,i}}{z_{t,i}^c} & 1+Y_{t,i}^2 & -X_{t,i}Y_{t,i} & -X_{t,i} \end{bmatrix}, \tag{9}$$

with $z_{t,i}^c$ the third component of $\boldsymbol{p}_{t,i}^c = \boldsymbol{R}_t^c \boldsymbol{p}_{t,i}^t$, with $\boldsymbol{R}_t^c \in SO(3)$ the rotation matrix between Σ_t and Σ_c, and $\bar{\boldsymbol{R}}_c = \mathrm{diag}(\boldsymbol{R}_c, \boldsymbol{R}_c)$.

F. Differential kinematics of the object's image features

Suppose that the object carried by the robot arm has attached m_o visible feature points, and let $\boldsymbol{p}_{o,j}^o$, with $j = 1, \ldots, m_o$, the fixed position of the j-th points with respect to Σ_o. The corresponding image feature vector $\boldsymbol{s}_{o,j} = \begin{bmatrix} X_{o,j} & Y_{o,j} \end{bmatrix}^\mathrm{T} \in \mathbb{R}^2$ can be measured either in the image plane of the camera carried by the other arm, or through the robot arm kinematics. The former case is more robust with respect to calibration error of the system kinematics, while the latter case relaxes the field-of-view constraint. The time derivative of $\boldsymbol{s}_{o,j}$ is

$$\dot{\boldsymbol{s}}_{o,j} = \begin{bmatrix} \dot{X}_{o,j} \\ \dot{Y}_{o,j} \end{bmatrix} = \boldsymbol{L}_{o,j} \dot{\boldsymbol{p}}_{o,j}^c, \tag{10}$$

where

$$\boldsymbol{L}_{o,j} = \frac{1}{z_{o,j}^c} \begin{bmatrix} 1 & 0 & -X_{o,j} \\ 0 & 1 & -Y_{o,j} \end{bmatrix}. \tag{11}$$

Being $\boldsymbol{p}_{o,j}^o$ constant in Σ_o, its time derivative in Σ_c depends only from the velocity of Σ_o with respect to Σ_c as follows

$$\dot{\boldsymbol{p}}_{o,j}^c = \begin{bmatrix} \boldsymbol{I}_3 & -\boldsymbol{S}(\boldsymbol{R}_o^c \boldsymbol{p}_{o,j}^o) \end{bmatrix} \bar{\boldsymbol{R}}_c^\top (\boldsymbol{v}_o - \boldsymbol{v}_c), \tag{12}$$

where $\boldsymbol{S}(\cdot) \in \mathbb{R}^{3\times 3}$ is the skew-symmetric matrix representing the vectorial product. Substituting (12) and (11) into (10) yields

$$\dot{\boldsymbol{s}}_{o,j} = \boldsymbol{J}_{o,j} (\boldsymbol{v}_o - \boldsymbol{v}_c). \tag{13}$$

III. Control law

The block diagram of the proposed control scheme has a cascade structure (see Fig. 2) with an inner loop for the motion control and an external loop implementing the proposed visual-impedance control laws.

A. Cartesian motion control

In this section the tracking of the pose of the two end-effectors trajectories is addressed. The dynamic model (5) is represented by a set of n second-order coupled and nonlinear differential equations relating the generalized joint positions, velocities and accelerations to the propellers forces, the robot-arms joint torques, and the end-effector wrench. A well-known strategy to control such a mechanical system is the *inverse dynamics control*, which is aimed at linearizing and decoupling the UAM dynamics via feedback. Nonlinearities such as Coriolis and centrifugal forces, friction torques, and gravity generalized forces can be cancelled by adding these terms to the control input, while decoupling can be achieved by weighting the control input through the inertia matrix. According to this dynamic model-based compensation, the generalized input force is chosen as

$$\boldsymbol{u} = \boldsymbol{B}(\boldsymbol{\xi})\boldsymbol{\alpha} + \boldsymbol{C}(\boldsymbol{\xi}, \dot{\boldsymbol{\xi}})\dot{\boldsymbol{\xi}} + \boldsymbol{g}(\boldsymbol{\xi}) + \boldsymbol{J}^\top(\boldsymbol{\xi})\boldsymbol{h}_e, \tag{14}$$

where $\boldsymbol{\alpha} \in \mathbb{R}^n$ constitutes the new control input to be properly designed. Folding (14) into (5), and taking into account that $\boldsymbol{B}(\boldsymbol{\xi})$ is never singular, yields

$$\ddot{\boldsymbol{\xi}} = \boldsymbol{\alpha}, \tag{15}$$

which is a linear and decoupled system, where $\boldsymbol{\alpha}$ represents a resolved acceleration input of the generalized joint variables.

Equation (15) has been obtained under the assumption of perfect compensation of the terms in (5). This relies on the availability of an accurate dynamic model. In case of imperfect compensation, a mismatch occurs causing the presence of a disturbance term in (15), i.e. $\ddot{\boldsymbol{\xi}} = \boldsymbol{\alpha} - \boldsymbol{\delta}$, where $\boldsymbol{\delta} \in \mathbb{R}^n$ is mainly due to unmodeled dynamics, aerodynamics disturbances, and parameter uncertainties. An active compensation of such a term can be achieved by considering the momentum-based estimator proposed in [1], [15], [16] and it will thus not be considered in the following of this paper.

Since Equation (15) contains $\ddot{\boldsymbol{\xi}}$, it is appropriate to address the time derivative of (4),

$$\dot{\boldsymbol{v}} = \boldsymbol{J}(\boldsymbol{\xi})\ddot{\boldsymbol{\xi}} + \dot{\boldsymbol{J}}(\boldsymbol{\xi})\dot{\boldsymbol{\xi}}, \tag{16}$$

which provides the relationship between the joint accelerations and the end-effectors linear and angular accelerations. Hence, the new control input $\boldsymbol{\alpha}$ in (15) can be chosen as

$$\boldsymbol{\alpha} = \boldsymbol{J}^\dagger(\boldsymbol{\xi}) \left(\boldsymbol{a} - \dot{\boldsymbol{J}}(\boldsymbol{\xi})\dot{\boldsymbol{\xi}} \right) + \boldsymbol{\alpha}_n, \tag{17}$$

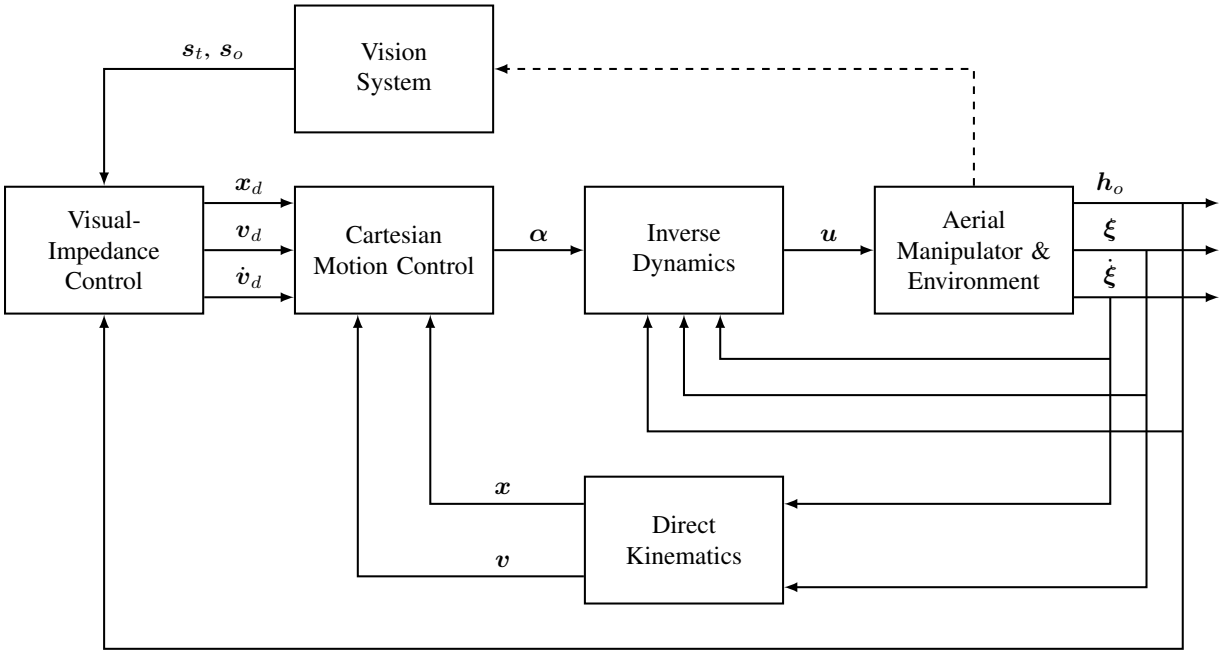

Fig. 2. Visual-impedance control scheme.

where $\boldsymbol{\alpha}_n \in \mathbb{R}^n$ denotes a generalized joint acceleration vector lying in the null space of $\boldsymbol{J}(\boldsymbol{\xi})$ which is available for redundancy resolution. In view of (16), this leads to

$$\dot{\boldsymbol{v}} = \boldsymbol{a}, \tag{18}$$

where $\boldsymbol{a} \in \mathbb{R}^{12}$ is a resolved acceleration in terms of end-effector variables. Deriving (17), a UAM moving in a singularity-free region of the robot arms's workspace is considered to compute the pseudo-inverse of the Jacobian. In case of presence of disturbances, Eq. (18) shall be modified into $\dot{\boldsymbol{v}} = \boldsymbol{a} - \boldsymbol{J}(\boldsymbol{\xi})\hat{\boldsymbol{\delta}}$, where $\hat{\boldsymbol{\delta}}$ is the estimated disturbance.

Let $\boldsymbol{x}_d = \begin{bmatrix}\boldsymbol{o}_{c,d}^\top & \boldsymbol{q}_{c,d}^\top & \boldsymbol{o}_{o,d}^\top & \boldsymbol{q}_{o,d}^\top\end{bmatrix}^\top \in \mathbb{R}^{14}$ be the desired pose of Σ_c and Σ_o in Σ_i. The desired orientations are expressed by using the unit quaternions corresponding to the desired rotation matrices $\boldsymbol{R}_{c,d}$ and $\boldsymbol{R}_{o,d}$. Moreover, let $\boldsymbol{v}_d = \begin{bmatrix}\dot{\boldsymbol{o}}_{c,d}^\top & \boldsymbol{\omega}_{c,d}^\top & \dot{\boldsymbol{o}}_{o,d}^\top & \boldsymbol{\omega}_{o,d}^\top\end{bmatrix}^\top \in \mathbb{R}^{12}$ and $\dot{\boldsymbol{v}}_d$ be the corresponding desired velocity and acceleration, respectively. A pose error between the desired and the actual arms end-effectors pose can be defined as $\tilde{\boldsymbol{x}} = \begin{bmatrix}\tilde{\boldsymbol{o}}_c^\top & \tilde{\boldsymbol{\epsilon}}_c^\top & \tilde{\boldsymbol{o}}_o^\top & \tilde{\boldsymbol{\epsilon}}_o^\top\end{bmatrix}^\top \in \mathbb{R}^{12}$, where $\tilde{\boldsymbol{o}}_c = \boldsymbol{o}_{c,d} - \boldsymbol{o}_c$, $\tilde{\boldsymbol{o}}_o = \boldsymbol{o}_{o,d} - \boldsymbol{o}_o$, and $\tilde{\boldsymbol{\epsilon}}_c \in \mathbb{R}^3$ and $\tilde{\boldsymbol{\epsilon}}_o \in \mathbb{R}^3$ are the vectorial parts of the quaternions corresponding to the rotation matrices $\boldsymbol{R}_{c,d}^\top \boldsymbol{R}_c$ and $\boldsymbol{R}_{o,d}^\top \boldsymbol{R}_o$, respectively. Hence, the resolved acceleration is chosen as

$$\boldsymbol{a} = \dot{\boldsymbol{v}}_d + \boldsymbol{K}_D \tilde{\boldsymbol{v}} + \boldsymbol{K}_P \tilde{\boldsymbol{x}}, \tag{19}$$

where $\tilde{\boldsymbol{v}} = \boldsymbol{v}_d - \boldsymbol{v}$, and $\boldsymbol{K}_D$ and $\boldsymbol{K}_P$ are suitable positive-definite gain matrices. Substituting (19) in (18) gives the closed-loop dynamic behaviour of the error

$$\dot{\tilde{\boldsymbol{v}}} + \boldsymbol{K}_D \tilde{\boldsymbol{v}} + \boldsymbol{K}_P \tilde{\boldsymbol{x}} = \boldsymbol{0}. \tag{20}$$

For the stability proof of (20) see [17].

B. Redundancy exploitation

The term $\boldsymbol{\alpha}_n$ in (17) is chosen to fully exploit the intrinsic redundancy of the UAM. Three secondary tasks have to be considered: 1) joint limits avoidance; 2) manipulability maximization; 3) vertical alignment of the center of gravity of the robot arms. More info can be found in [7] for the general formulation of $\boldsymbol{\alpha}_n$, and in [18] for the definition of these secondary tasks.

C. Image-based visual-impedance control

Assuming that at least four coplanar, but not collinear, image features are employed for both the target structure on the ground and the carried object, the poses of Σ_t and Σ_o are univocally determined by the image projection $\boldsymbol{s}_t = \begin{bmatrix}\boldsymbol{s}_{t,1}^\top & \cdots & \boldsymbol{s}_{t,m_t}^\top\end{bmatrix}^\top$ and $\boldsymbol{s}_o = \begin{bmatrix}\boldsymbol{s}_{o,1}^\top & \cdots & \boldsymbol{s}_{o,m_o}^\top\end{bmatrix}^\top$ of the corresponding image features [19]. It is also assumed that $m_t = m_o = m$, with $m \geq 4$, and $\boldsymbol{s}_t = \boldsymbol{s}_o$ when the desired relative pose between Σ_t and Σ_o is reached, e.g., when the object is perfectly plugged into the target. This assumption can always be guaranteed if the image features $\boldsymbol{s}_o$ are virtualized through the direct kinematics of the robot, as explained in Section II-F. In order to make the UAM capable of autonomously positioning the carried object on the target structure, the following image error is proposed

$$\tilde{\boldsymbol{s}} = \boldsymbol{s}_o - \boldsymbol{s}_t. \tag{21}$$

The control objective is the nullification of $\tilde{\boldsymbol{s}}$ and the achievement of a desired behaviour of the interaction wrench between the object and the target. Differentiating (21) and taking into

account (8) and (13), yields

$$\begin{aligned}\dot{\tilde{\boldsymbol{s}}} &= \dot{\boldsymbol{s}}_o - \dot{\boldsymbol{s}}_t \\ &= \boldsymbol{J}_o(\boldsymbol{v}_o - \boldsymbol{v}_c) - \boldsymbol{J}_t\boldsymbol{v}_c \\ &= \boldsymbol{J}_o\boldsymbol{v}_o - (\boldsymbol{J}_t + \boldsymbol{J}_o)\boldsymbol{v}_c, \\ &= \boldsymbol{J}_o\boldsymbol{v}_o - \boldsymbol{J}_c\boldsymbol{v}_c,\end{aligned} \tag{22}$$

where $\boldsymbol{J}_o = \begin{bmatrix}\boldsymbol{J}_{o,1}^\top & \cdots & \boldsymbol{J}_{o,m}^\top\end{bmatrix}^\top \in \mathbb{R}^{2m\times 6}$, $\boldsymbol{J}_t = \begin{bmatrix}\boldsymbol{J}_{t,1}^\top & \cdots & \boldsymbol{J}_{t,m}^\top\end{bmatrix}^\top \in \mathbb{R}^{2m\times 6}$, and $\boldsymbol{J}_c = \boldsymbol{J}_t + \boldsymbol{J}_o$.

In the proposed control architecture shown in Fig. 2, the Cartesian motion control action is purposefully made stiff so as to enhance disturbance rejection but, rather than ensuring tracking of the desired end-effectors pose, it shall ensure tracking of a reference pose resulting from the visual-impedance control action (i.e., *compliant reference frame*). Hence, it is worth computing the reference trajectory specified by $\boldsymbol{o}_{o,d}$, $\boldsymbol{q}_{o,d}$ and $\boldsymbol{v}_{o,d}$ taking in account both the interaction wrench (compliant behaviour) and the visual error (positioning task).

1) First-order image-based visual-interaction control law based on the system Jacobian-matrix transpose (FoJt): The proposed image-based visual-interaction control law is chosen so as to enforce an equivalent virtual damper-spring behavior for the pose displacement driven by the visual error in the image plane when the object exerts a wrench $\boldsymbol{h}_o$ on the environment. Consider the following interaction equation

$$\boldsymbol{D}_o\boldsymbol{v}_{o,d} + \boldsymbol{\sigma} = \boldsymbol{h}_o, \tag{23}$$

where $\boldsymbol{D}_o$ is positive matrix corresponding to a virtual dumping, and $\boldsymbol{\sigma} \in \mathbb{R}^6$ is a terms to be designed for nullifying the visual error. Consider the Lyapunov function candidate

$$V(\tilde{\boldsymbol{s}}) = \frac{1}{2}\tilde{\boldsymbol{s}}^\top k_s\tilde{\boldsymbol{s}}. \tag{24}$$

The time derivative of (24) is

$$\begin{aligned}\dot{V} &= \tilde{\boldsymbol{s}}^\top k_s\dot{\tilde{\boldsymbol{s}}} \\ &= \tilde{\boldsymbol{s}}^\top k_s\left(\boldsymbol{J}_o\boldsymbol{v}_o - \boldsymbol{J}_c\boldsymbol{v}_c\right) \\ &= \tilde{\boldsymbol{s}}^\top k_s\left(\boldsymbol{J}_o\boldsymbol{D}_o^{-1}\left(\boldsymbol{h}_o - \boldsymbol{\sigma}\right) - \boldsymbol{J}_c\boldsymbol{v}_c\right),\end{aligned} \tag{25}$$

where, with a small abuse of notation, we used $\boldsymbol{v}_o$ in reason of $\boldsymbol{v}_{o,d}$. The following control law is thus designed

$$\boldsymbol{\sigma} = \boldsymbol{D}_o\left(\boldsymbol{K}\boldsymbol{J}_o^\top k_s\tilde{\boldsymbol{s}} - \boldsymbol{J}_o^\dagger\boldsymbol{J}_c\boldsymbol{v}_c\right), \tag{26}$$

where $\boldsymbol{K}$ is positive definite matrix and $k_s > 0$ a positive gain. Replacing (26) in (25) yields

$$\dot{V} = \tilde{\boldsymbol{s}}^\top k_s\boldsymbol{J}_o\boldsymbol{D}_o^{-1}\boldsymbol{h}_o - \tilde{\boldsymbol{s}}^\top k_s\boldsymbol{J}_o\boldsymbol{K}\boldsymbol{J}_o^\top k_s\tilde{\boldsymbol{s}}. \tag{27}$$

In absence of interaction ($\boldsymbol{h}_o = \boldsymbol{0}$), for any trajectory, the Lyapunov function decreases as long as $\tilde{\boldsymbol{s}} \neq \boldsymbol{0}$, i.e., the system (23) is *asymptotically stable*. The system then reaches an equilibrium state determined by $\boldsymbol{J}_o^\top k_s\tilde{\boldsymbol{s}} = \boldsymbol{0}$. From (21) it can be recognized that, under the assumption of *full-rank* Jacobian $\boldsymbol{J}_o$, it is $\tilde{\boldsymbol{s}} = \boldsymbol{s}_o - \boldsymbol{s}_t = \boldsymbol{0}$, i.e., the sought result. When $\mathcal{N}(\boldsymbol{J}_o^\top) \neq \emptyset$, the function (27) is only negative semi-definite, since $\dot{V} = 0$ for $\tilde{\boldsymbol{s}} \neq \boldsymbol{0}$ with $k_s\tilde{\boldsymbol{s}} \in \mathcal{N}(\boldsymbol{J}_o^\top)$. In this case the algorithm can get stuck. However, this situation occurs only if the end-effector cannot move in the direction required to nullify the visual error from the current robot configuration. These robot configurations correspond to kinematic singularities that can be generated, for example, when some links are aligned. However, for a redundant sistem, like a UAM, singular configurations can be actively avoided by introducing a specific secondary task via term $\boldsymbol{\alpha}_n$ term in (17) (see [12], [20]).

In case of interaction, replacing (26) in (23) yields

$$\boldsymbol{D}_o\boldsymbol{v}_{o,d} + \boldsymbol{K}_o\Delta\boldsymbol{x}_s = \boldsymbol{h}_o, \tag{28}$$

where $\boldsymbol{K}_o = \boldsymbol{D}_o\boldsymbol{K}$ is a Cartesian stiffness matrix, and $\Delta\boldsymbol{x}_s = \boldsymbol{J}_o^\top k_s\tilde{\boldsymbol{s}} - \boldsymbol{K}^{-1}\boldsymbol{J}_o^\dagger\boldsymbol{J}_c\boldsymbol{v}_c$ represents the Cartesian offset of a virtual spring driven by the error in the image plane $\tilde{\boldsymbol{s}}$ purged of the apparent visual error generated by the camera motion.

At the equilibrium, it is

$$\boldsymbol{h}_o = \boldsymbol{K}_o\boldsymbol{J}_o^\top k_s\tilde{\boldsymbol{s}}, \tag{29}$$

where $\boldsymbol{J}_o^\top$ maps the image error to a Cartesian offset.

2) First-order image-based visual-interaction control law based on the system Jacobian-matrix inverse (FoJi): Considering (25), the following control input is chosen

$$\boldsymbol{\sigma} = \boldsymbol{D}_o\left(\boldsymbol{K}\boldsymbol{J}_o^\dagger k_s\tilde{\boldsymbol{s}} - \boldsymbol{J}_o^\dagger\boldsymbol{J}_c\boldsymbol{v}_c\right). \tag{30}$$

Replacing (30) in (25) yields

$$\dot{V} = \tilde{\boldsymbol{s}}^\top k_s\boldsymbol{J}_o\boldsymbol{D}_o^{-1}\boldsymbol{h}_o - \tilde{\boldsymbol{s}}^\top k_s\boldsymbol{J}_o\boldsymbol{K}\boldsymbol{J}_o^\dagger k_s\tilde{\boldsymbol{s}}. \tag{31}$$

In absence of interaction ($\boldsymbol{h}_o = \boldsymbol{0}$) and singularities in $\boldsymbol{J}_o$, the Lyapunov function decreases as long as $\tilde{\boldsymbol{s}} \neq \boldsymbol{0}$, i.e., the system is *asymptotically stable* and reaches the desired equilibrium posture with $\tilde{\boldsymbol{s}} = \boldsymbol{0}$.

In case of interaction, replacing (30) in (23) yields (28) with $\Delta\boldsymbol{x}_s = \boldsymbol{J}_o^\dagger k_s\tilde{\boldsymbol{s}} - \boldsymbol{K}^{-1}\boldsymbol{J}_o^\dagger\boldsymbol{J}_c\boldsymbol{v}_c$. The gain k_s determines the convergence rate of the visual error, while through the matrices $\boldsymbol{K}$ and $\boldsymbol{D}_o$ it is possible to regulate the desired interaction compliance in the Cartesian space.

3) Second-order visual-impedance control law (SoVI): Consider the following interaction equation

$$\boldsymbol{M}_o\dot{\boldsymbol{v}}_{o,d} + \boldsymbol{D}_o\boldsymbol{v}_{o,d} + \boldsymbol{K}\boldsymbol{J}_o^\top\left(k_s\tilde{\boldsymbol{s}} + \boldsymbol{J}_c\boldsymbol{v}_c\right) = \boldsymbol{h}_o, \tag{32}$$

where $\boldsymbol{M}_o$, $\boldsymbol{D}_o$, and $\boldsymbol{K}$ are symmetric positive matrices corresponding to the virtual mass, dumping, and stiffness, respectively. Consider the positive definite Lyapunov function candidate

$$V(\tilde{\boldsymbol{s}}, \boldsymbol{v}_o) = \frac{1}{2}\tilde{\boldsymbol{s}}^\top k_s\tilde{\boldsymbol{s}} + \frac{1}{2}\boldsymbol{v}_o^\top\boldsymbol{K}^{-1}\boldsymbol{M}_o\boldsymbol{v}_o. \tag{33}$$

The time derivative of (33) is

$$\begin{aligned}\dot{V} &= \dot{\tilde{\boldsymbol{s}}}^\top k_s\tilde{\boldsymbol{s}} + \boldsymbol{v}_o^\top\boldsymbol{K}^{-1}\boldsymbol{M}_o\dot{\boldsymbol{v}}_o \\ &= \left(\boldsymbol{v}_o^\top\boldsymbol{J}_o^\top - \boldsymbol{v}_c^\top\boldsymbol{J}_c^\top\right)k_s\tilde{\boldsymbol{s}} \\ &\quad + \boldsymbol{v}_o^\top\boldsymbol{K}^{-1}\left(\boldsymbol{h}_o - \boldsymbol{D}_o\boldsymbol{v}_o - \boldsymbol{K}\boldsymbol{J}_o^\top\left(k_s\tilde{\boldsymbol{s}} + \boldsymbol{J}_c\boldsymbol{v}_c\right)\right) \\ &= \boldsymbol{v}_o^\top\boldsymbol{K}^{-1}\boldsymbol{h}_o - \boldsymbol{v}_o^\top\boldsymbol{K}^{-1}\boldsymbol{D}_o\boldsymbol{v}_o + \boldsymbol{v}_c^\top\boldsymbol{J}_c^\top\left(k_s\tilde{\boldsymbol{s}} - \boldsymbol{J}_o\boldsymbol{v}_o\right).\end{aligned} \tag{34}$$

When the camera stops and in absence of interaction, the Lyapunov function decreases as long as $\boldsymbol{v}_o \neq \boldsymbol{0}$, and $\tilde{\boldsymbol{s}} = \boldsymbol{0}$ due to (32). In case of interaction with the environment, the system reaches the equilibrium posture determined by (32):

$$\boldsymbol{h}_o = \boldsymbol{K}\boldsymbol{J}_o^\top k_s\tilde{\boldsymbol{s}}. \tag{35}$$

D. Eye-hand motion coordination

The camera motion is commanded in a decoupled way with respect to the object motion, but the corresponding motion is taken into account as shown in (26), (30), and (32). The desired velocity command $\boldsymbol{v}_c$ is generated through two concurrent objectives: 1) push the centroid of the image features in the center of the image; 2) maximize the image feature expansion in the image by generating an attractive field towards the image limits, which is counterbalanced by a repulsive barrier function, which is activated when an image feature becomes too close to the image borders. Details are omitted for brevity.

IV. Simulation

The proposed control laws have been tested in simulation by using V-Rep and Matlab. The former simulates the system dynamics and the physical interaction with the environment. The latter implements the proposed cascade control laws. The evolution of the two environments is interlocked ensuring a proper time synchronization, with the control loop running at 5 ms and a camera frame rate of 25 Hz.

An X8 drone is endowed with two KINOVA MICO^2 6-DoF robot arms, as shown in Fig. 1. A camera is attached to the left arm, while a peg (conical pyramid) is attached through a wrist force sensor to the right arm. A hole is fixed on the ground. The goal consists in inserting the peg into a fixed hole starting from an assigned initial configuration using only visual and force measurements.

Four point image features fixed with the hole are considered in a square configuration, while four virtual image features are generated by using the robot-arm direct kinematics. The virtual image features of the peg are generated in a way to be coincident with the hole image features when the peg is virtually inserted 2 cm beyond the end along the vertical axis (z-axis) and 2 degrees around the y-axis the corresponding physical limits. In this way it is simulated an error in the desired relative assembling configuration, so as to test the effectiveness of the proposed control schemes also at the steady state. In fact, this means that the visual error cannot reach zero and, without a proper interaction control law, a high interaction force might be generated.

Both visual and force sensors have been characterized with an additive white Gaussian noise to a magnitude inspired by real instruments (2 pixels and 2 N/0.05 Nm, respectively). The UAV low-level control law has been tuned in a way to achieve an attitude settling time of 1 s and an overshoot less than 20 % (3 s for the position control without overshoot), while the settling time of the position control of the robot-arm joints is 0.5 s.

The control laws have been tested comparatively by tuning control gains to achieve a similar settling time and residual force at steady state:

- FoJt: $k_s = 0.02$, $\boldsymbol{K} = \text{diag}(0.1, 0.1, 0.4, 10, 10, 15)$, $\boldsymbol{D}_o = \text{diag}(100, 100, 800, 25, 25, 50)$.
- FoJi: $k_s = 0.01$, $\boldsymbol{K} = \text{diag}(5, 5, 30, 15, 15, 25)$, $\boldsymbol{D}_o = \text{diag}(250, 250, 2000, 15, 15, 25)$.
- SoVI: $k_s = 1$, $\boldsymbol{K} = \text{diag}(1, 1, 5.5, 4, 4, 2)$, $\boldsymbol{M}_o = \text{diag}(1, 1, 5, 0.5, 0.5, 0.25)$, $\boldsymbol{D}_o = \text{diag}(100, 100, 250, 2, 2, 1)$.

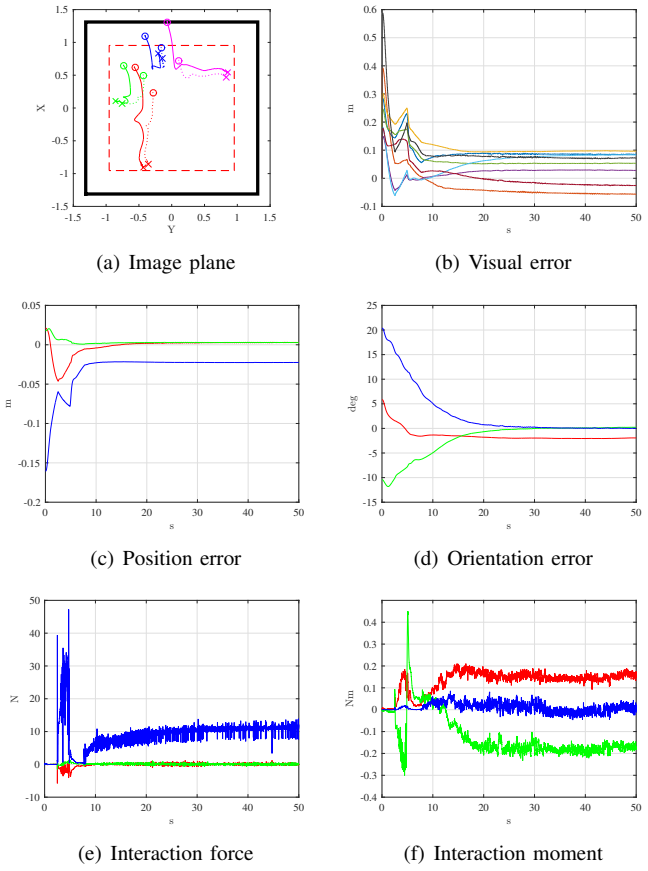

(a) Image plane (b) Visual error

(c) Position error (d) Orientation error

(e) Interaction force (f) Interaction moment

Fig. 3. Results achieved with the FoJt control law.

The results achieved with the FoJt control law are shown in Fig. 3. The motion of the image features in the image plane are shown in Fig. 3(a), with solid lines the hole's features and with dotted lines the peg's features. The cross symbols indicate the final positions of each image feature, while the circle symbols indicate the initial positions. One can notice that in the final configuration the image features are close to the image borders (solid black line) by keeping a safe distance (red dotted line) thanks to the adopted barrier function. In this way, the observation of the object features is optimized. As expected, the final configuration does not nullify the visual error, as it is more clearly shown in Fig. 3(b). The interaction force and moment are shown in Figs. 3(e) and 3(f), respectively (red, green, and blue is the adopted sequence of color for the x, y, and z components). One can notice a peak at about 5 s, when the peg collides with the hole border due to the initial position error and to the nonlinear mapping of the visual error to the Cartesian motion. Nevertheless, in few seconds the peg moves towards the hole and falls inside it. At the steady state, a final interaction force of about 10 N along the z-axis exists due to the assigned offset of 2 cm. Similarly for the residual moments due to the assigned offset of 2 degrees. In fact, Figs. 3(c) and 3(d) show the position and orientation error (angle-axis representation), respectively, with respect to the desired relative pose of the peg with respect to the hole. One can notice, for example, how a residual error of 2 cm in position along the z-axis persists as expected. Despite this error in the reference pose, the interaction force remains

limited and stable. Similar consideration can be made for the interaction moment.

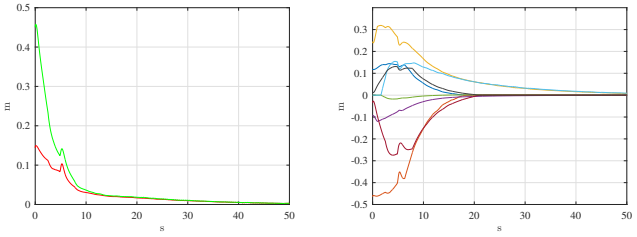

(a) Image-features centroid error. (b) Image-features expansion error

Fig. 4. Camera task errors.

The errors of the tasks employed for the camera motion control are shown in Fig. 4. Figure 4(a) shows the visual error of the image features center with respect to the image center, while the distance of the image features components with respect to the image borders is shown in Fig. 4(b). Red dotted lines in Fig. 3(a) represent the chosen safe distance from the borders. In both cases a smooth nullification of the errors is archived.

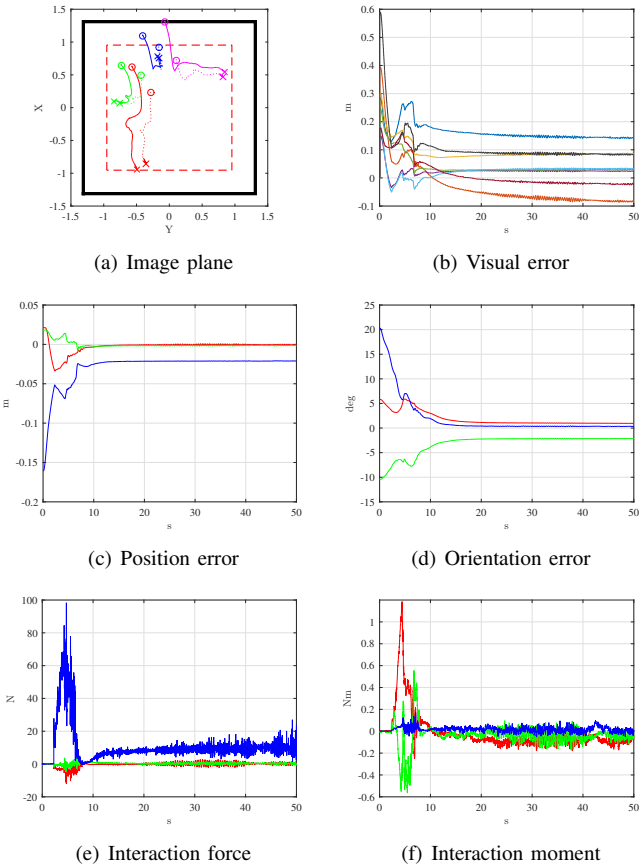

(a) Image plane (b) Visual error

(c) Position error (d) Orientation error

(e) Interaction force (f) Interaction moment

Fig. 5. Results achieved with the FoJi control law.

The results achieved with the FoJi control law are shown in Fig. 5. The system behaviour is close to the previous one but with a higher intrinsic stiffness. One can notice that the impact on the border of the hole determines a higher force, while the steady state interaction force is similar to the previous case. With the tuned control gains it has not been possible achieving a smoother behaviour during the initial impact without affecting also the steady state.

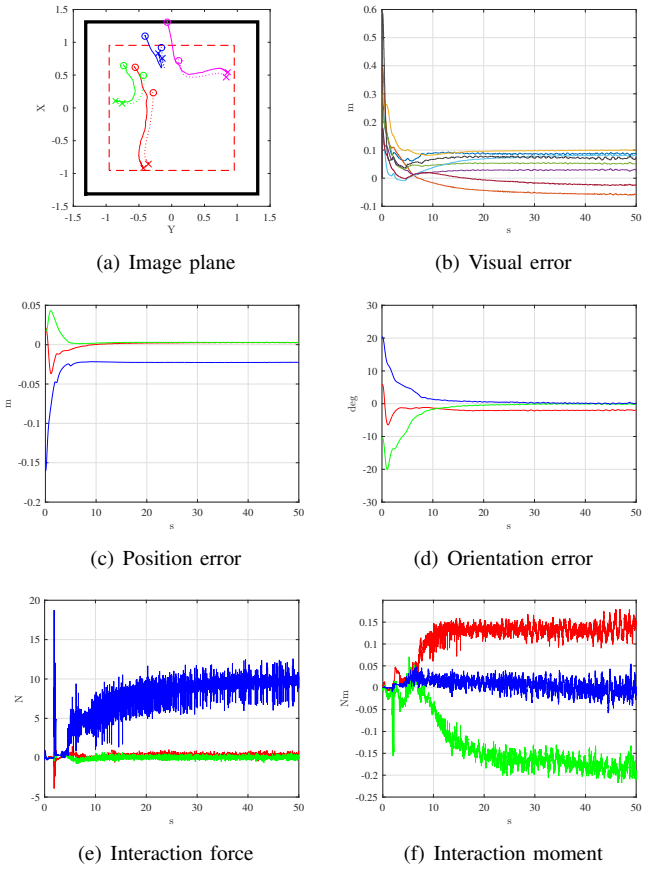

(a) Image plane (b) Visual error

(c) Position error (d) Orientation error

(e) Interaction force (f) Interaction moment

Fig. 6. Results achieved with the SoVI control law.

Finally, the SoVI control law provides the better results overall, as shown in Fig. 6. Thanks to the increased number of control gains which are available to tune the desired behaviour, it has been possible to avoid the initial impact and to achieve a smooth insertion of the peg into the hole. With this control modality, the tuning phase is easier due to the physical meaning of most of the control gains. In fact, only the virtual spring has a nonlinear coupling with the visual error, while the remaining parameters (mass and damping) are expressed directly in the Cartesian space.

A comparison between the proposed methods is shown in Fig. 7. The achieved behaviours are similar, thanks to a suitable tuning phase, but the SoVI approach allows to better control the Cartesian motion avoiding the impact with the hall border. Moreover, the FoJi approach is more sensible to force/moment noise and, in general, it requires more time to be properly tuned.

V. Conclusion and Future Work

Three novel image-based visual-impedance control laws suitably designed for dual-arm UAMs have been presented and tested through simulations: first-order interaction equations based on system Jacobian-matrix transpose and inverse, and a second-order visual-impedance control law. Differently

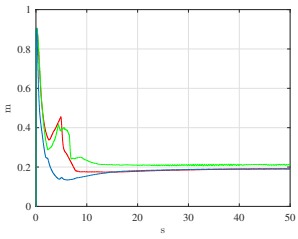

(a) Norm of the visual error

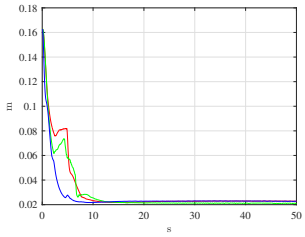

(b) Norm of the position error

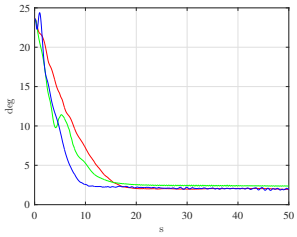

(c) Norm of the orientation error

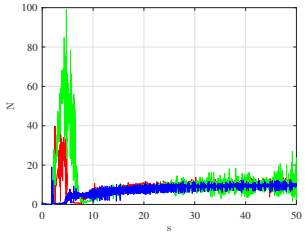

(d) Norm of the interaction force

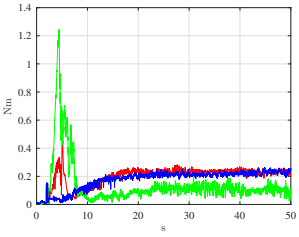

(e) Norm of the interaction moment

Fig. 7. Comparison of the achieved results (in norm): FoJt in red, FoJi in green, and SoVI in blue.

from other approaches, suitable visual errors have been designed through the image-based paradigm generating an elastic wrench component. Visual measures are also employed to coordinate the eye-in-hand camera motion with the execution of the manipulation task performed with the second arm carrying an object. Simulation results confirm the effectiveness of the proposed solutions.

Real experiments will be carried out as future work as soon as the experimental setup will be ready. At that time, suitable visual elaboration algorithm capable to cope with real environment and textures will be considered. Moreover, the possibility of increasing the update-rate of the visual measurements through a prediction based on a Kalman filter implementation with IMU and joint data will be investigated.

REFERENCES

[1] F. Ruggiero, J. Cacace, H. Sadeghian, and V. Lippiello, "Passivity-based control of VToL UAVs with a momentum-based estimator of external wrench and unmodeled dynamics," *Robotics and Autonomous Systems*, vol. 72, pp. 139 – 151, 2015.

[2] M. Fumagalli, S. Stramigioli, and R. Carloni, "Mechatronic design of a robotic manipulator for unmanned aerial vehicles," in *2016 IEEE/RSJ Int. Conf. on Intelligent Robots and Systems (IROS)*, Oct 2016, pp. 4843–4848.

[3] C. D. Bellicoso, L. R. Buonocore, V. Lippiello, and B. Siciliano, "Design, modeling and control of a 5-DoF light-weight robot arm for aerial manipulation," in *2015 23rd Mediterranean Conference on Control and Automation (MED)*, June 2015, pp. 853–858.

[4] A. Suarez, A. E. Jimenez-Cano, V. M. Vega, G. Heredia, A. Rodrguez-Castao, and A. Ollero, "Lightweight and human-size dual arm aerial manipulator," in *2017 Int. Conf. on Unmanned Aircraft Systems (ICUAS)*, June 2017, pp. 1778–1784.

[5] J. L. J. Scholten, M. Fumagalli, S. Stramigioli, and R. Carloni, "Interaction control of an UAV endowed with a manipulator," in *2013 IEEE Int. Conf. on Robotics and Automation*, May 2013, pp. 4910–4915.

[6] F. Forte, R. Naldi, A. Macchelli, and L. Marconi, "Impedance control of an aerial manipulator," in *2012 American Control Conference (ACC)*, June 2012, pp. 3839–3844.

[7] V. Lippiello and F. Ruggiero, "Cartesian impedance control of a UAV with a robotic arm," in *10th IFAC Symposium on Robot Control*, Sep 2012, pp. 704–709.

[8] ——, "Exploiting redundancy in Cartesian impedance control of UAVs equipped with a robotic arm," in *IEEE/RSJ Int. Conf. on Intelligent Robots and Systems*, Oct 2012, pp. 3768–3773.

[9] H. Sayyaadi and M. Sharifi, "Adaptive impedance control of UAVs interacting with environment using a robot manipulator," in *2014 Second RSI/ISM Int. Conf. on Robotics and Mechatronics (ICRoM)*, Oct 2014, pp. 636–641.

[10] E. Cataldi, G. Muscio, M. A. Trujillo, Y. Rodriguez, F. Pierri, G. Antonelli, F. Caccavale, A. Viguria, S. Chiaverini, and A. Ollero, "Impedance control of an aerial-manipulator: Preliminary results," in *2016 IEEE/RSJ Int. Conf. on Intelligent Robots and Systems (IROS)*, Oct 2016, pp. 3848–3853.

[11] V. Lippiello, B. Siciliano, and L. Villani, "A position-based visual impedance control for robot manipulators," in *Proceedings 2007 IEEE International Conference on Robotics and Automation*, April 2007, pp. 2068–2073.

[12] B. Siciliano, L. Sciavicco, and L. Villani, *Robotics: modelling, planning and control*, ser. Advanced Textbooks in Control and Signal Processing. London: Springer, 2009.

[13] K. Nonami, F. Kendoul, S. Suzuki, W. Wang, and D. Nakazawa, *Autonomous Flying Robots: Unmanned Aerial Vehicles and Micro Aerial Vehicles*, 1st ed. Springer Publishing Company, Incorporated, 2010.

[14] F. Chaumette and S. Hutchinson, "Visual servo control. I. Basic approaches," *IEEE Robotics Automation Magazine*, vol. 13, no. 4, pp. 82–90, Dec 2006.

[15] F. Ruggiero, M. A. Trujillo, R. Cano, H. Ascorbe, A. Viguria, C. Peréz, V. Lippiello, A. Ollero, and B. Siciliano, "A multilayer control for multirotor UAVs equipped with a servo robot arm," in *2015 IEEE Int. Conf. on Robotics and Automation (ICRA)*, May 2015, pp. 4014–4020.

[16] F. Ruggiero, J. Cacace, H. Sadeghian, and V. Lippiello, "Impedance control of VToL UAVs with a momentum-based external generalized forces estimator," in *2014 IEEE Int. Conf. on Robotics and Automation (ICRA)*, May 2014, pp. 2093–2099.

[17] F. Caccavale, C. Natale, B. Siciliano, and L. Villani, "Resolved-acceleration control of robot manipulators: A critical review with experiments," *Robotica*, vol. 16, no. 5, p. 565573, 1998.

[18] V. Lippiello, J. Cacace, A. Santamaria-Navarro, J. Andrade-Cetto, M. . Trujillo, Y. R. Esteves, and A. Viguria, "Hybrid visual servoing with hierarchical task composition for aerial manipulation," *IEEE Robotics and Automation Letters*, vol. 1, no. 1, pp. 259–266, Jan 2016.

[19] S. Hutchinson, G. D. Hager, and P. I. Corke, "A tutorial on visual servo control," *IEEE Transactions on Robotics and Automation*, vol. 12, no. 5, pp. 651–670, Oct 1996.

[20] G. Antonelli, "Stability analysis for prioritized closed-loop inverse kinematic algorithms for redundant robotic systems," *IEEE Transactions on Robotics*, vol. 25, no. 5, pp. 985–994, 2009.